Resolving luminescence in spatial and compositional domains

Thomsen, K.J.; Kook, M.; Murray, A.S.; Jain, M.

Published in:
Radiation Measurements

Link to article, DOI:
10.1016/j.radmeas.2018.06.002

Publication date:
2018

Document Version
Publisher's PDF, also known as Version of record

Radiation Measurements 120 (2018) 260–266

Contents lists available at ScienceDirect

Radiation Measurements

journal homepage: www.elsevier.com/locate/radmeas

Resolving luminescence in spatial and compositional domains

K.J. Thomsen[a,*], M. Kook[a], A.S. Murray[b], M. Jain[a]

[a] Center for Nuclear Technologies, Technical University of Denmark, DTU Risø Campus, Denmark
[b] Nordic Laboratory for Luminescence Dating, Department of Geoscience, Aarhus University, Risø Campus, Denmark

ABSTRACT

It is desirable to be able to establish the relationship between the spatial distribution of luminescence and chemical composition/mineralogy. This is especially true in complex, heterogeneous samples such as solid coarse-grained rock slices and separated feldspar grains, where the internal dose rate is very dependent on the effective size of luminescent regions of the sample. The addition of spectral information would then help to give further insights into luminescence production mechanisms.

A high sensitivity imaging attachment to the Risø TL/OSL Reader for investigating the spatial distribution of OSL and TL from natural and artificial phosphors has recently been developed (Kook et al., 2015). When combined with a Bruker μ-XRF facility and a high sensitivity spectrometer attachment, it is possible to investigate the relationship between the spatial distribution of luminescence, the distribution of chemical composition/mineralogy and the associated excitation and emission spectra.

Here laboratory measurements undertaken using solid rock samples are presented and the observed relationships and their dosimetric implications are discussed.

1. Introduction

In luminescence dating two quantities need to be determined: the absorbed dose and the dose rate. When determining the dose rate in sediments we need to consider the alpha dose rate from short range (~40 μm) heavy charged particles (helium nucleii), the beta dose rate from longer range (~2 mm) electrons, the gamma dose rate from (~30 cm) photons and the cosmic ray dose rate, which is a mixture of light and heavy particles and photons. Due to their short range, the main source of internal dose rate within grains is alpha and beta particles, whereas the external dose rate derives mainly from beta particles and gamma rays, as well as cosmic rays (usually a small % of the total, Prescott and Hutton, 1994). If the dosimeter is potassium-rich, the internal dose rate from beta particles from ^{40}K is significant; typically 30–40% of the total dose rate. Nevertheless, it has proved very difficult to establish experimentally the expected correlation between equivalent dose in potassium-rich feldspar grains and potassium content and grain size (e.g Trauerstein et al., 2012; Smedley and Pearce, 2016; Buylaert et al., these proceedings).

In rock surface dating in particular, it is important that methods enabling the localisation of the origins of the luminescence signal in a matrix of various sources of light and ionising radiation are developed. In a solid matrix made up of various mineral grains the microdosimetric variations from grain to grain will be a function of grain size and internal activity.

In this paper, spatially resolved luminescence images from four solid rock slices are compared with the spatial distribution of major element concentrations. Rocks are in general much more mineralogically diverse than weathered sediments; in particular, concentrations of Ca- and Na-feldspars will tend to be significantly higher. Thus, it is more likely that significant luminescence will derive from all regions of the feldspar ternary diagram. As a result, these investigations are aimed at determining the origin of luminescence signals in slices of solid rock. The luminescence signals considered here are optically stimulated luminescence (OSL), infrared stimulated luminescence (IRSL) measured at 50 °C (IR_{50}) and at 225 °C immediately after the preceding IR_{50} measurement (i.e. $pIRIR_{225}$; Thomsen et al., 2008), infrared photostimulated luminescence (IRPL; Prasad et al., 2017) and thermoluminescence (TL).

2. Experimental details

2.1. Instrumentation

All luminescence experiments used an automated Risø TL/OSL DA-20 Reader (Bøtter-Jensen et al., 2010; Lapp et al., 2015) equipped with a calibrated ^{90}Sr/^{90}Y beta source as the measurement platform. Optical stimulation is achieved using blue (470 ± 20 nm, ~80 mW/cm^2) or

* Corresponding author.
E-mail address: krth@dtu.dk (K.J. Thomsen).

https://doi.org/10.1016/j.radmeas.2018.06.002
Received 15 December 2017; Received in revised form 27 March 2018; Accepted 2 June 2018
Available online 04 June 2018

infrared (IR, 850 ± 30 nm, ~300 mW/cm^2) light emitting diodes (LEDs). Detection of luminescence signals used 1) a standard photomultiplier tube (PMT), 2) a high-sensitivity spectrometer, or 3) an EMCCD imaging system.

The PMT is a blue/UV sensitive tube (PDM9107Q-AP-TTL-03 with quartz window), which has a spectral range of 160–630 nm with maximum detection efficiency between 200 and 400 nm.

The spatially resolved luminescence images were measured using a high sensitivity-luminescence imaging-system based on an EMCCD camera (Kook et al., 2015; Thomsen et al., 2015) coupled to a Risø TL/OSL Reader; the imaging system includes an automatic motorized self-focusing unit. Kook et al. (2015) describe an acromatic lens system in which the focusing is relatively independent of wavelength, but this at the expense of UV sensitivity. Instead, to maximise UV sensitivity, it was chosen to use a fused-silica lens combination. Because the focusing plane in this system is wavelength dependent the automated focusing uses three LEDs (470 nm, 525 nm and 870 nm) as illumination sources. Sample thickness and/or vertical position also affects the location of the focal plane. The automatic focusing module uses a low-noise piezoelectric linear motor capable of providing focusing precision down to 0.5 μm. The focusing module also includes a motorized aperture adjustment function to increase the dynamic range, allowing the measurement of both very dim and very bright samples. Images are captured by a Peltier cooled (−80 °C) Evolve EMCCD camera (Photometrics). The EMCCD has a broadband (UV to Near IR, UV-enhanced) window and a high quantum efficiency compared to a PMT.

The Risø high sensitivity emission spectrometer enables measurement of both TL and OSL emission luminescence spectra (Prasad et al., 2016). It is based on an Andor EMCCD Camera, a Shamrock 193 imaging spectrograph base unit and 193i ruled gratings a 300 l/mm (500 nm blaze), and a 150 l/mm (500 nm) blaze giving wavelength regions of e.g. 300–700 nm and 300–850 nm (centre wavelength adjustable), mounted on a motorized dual grating turret. The spectrometer is coupled to a Risø TL/OSL Reader using a specially designed optical 3.1 mm circular fibre bundle with 114 UV-VIS-NIR transmission fibres, each 200 μm in diameter, with a numerical aperture of 0.22. Fibres are arranged in a rectangular form at the spectrometer end (2 × 57) and circular form at the sample end.

Based on the known TL and OSL emission spectra of quartz and feldspar (e.g. Huntley et al., 1991; Bøtter-Jensen et al., 1994; see also Fig. S1) the PMT and the EMCCD camera measure TL, OSL and IRSL signals through either 5 mm of a coated Hoya U-340 glass filter (UV detection) or through 3 mm of BG3 and 4 mm of BG39 glass filters (Blue detection). UV detection was used for quartzite and blue detection for the other rock types.

To analyse major element concentrations a μXRF instrument (Brüker M4 Tornado μXRF) is used; this enables semi-quantitative analysis based on fundamental parameters. The X-ray spot size is 13.7 μm at Mo (K_α) and 33.1 μm at Mo (L). A qualitative elemental map was first obtained by scanning the entire surface of the sample. This map identified high concentration regions. The concentrations in these regions were quantified by measuring a least three randomly placed spots with acquisition times of 45 s using a single Rh target X-ray tube (600 μA, 50 kV) focussed to a spot size of ~25 μm by polycapillary lens optics.

The calibration for the μXRF is based on fundamental parameter-based (standardless) quantification algorithms (Flude et al., 2017). The general validity of this calibration has been confirmed using reagent grade KCO_2, $NaCO_2$, $CaCO_3$, SiO_2 and Al_2O_3 powders, but no attempts have been made to correct for matrix or grain size/shape effects in real samples. Results are summarised in Table S1.

2.2. Samples

We present measurements from four different rock slices (ø = 9.7 mm and thickness ~1 mm): 1) quartzite 2) alkali feldspar (orthoclase from Evje, Norway) 3) granite I from an archaeological stone pier on Fyn, Denmark and 4) granite II from a granitic rock from a modern beach near Roskilde, Denmark.

2.3. Measurement protocols

All measurements presented here make use of laboratory generated (using $^{90}Sr/^{90}Y$ beta sources) luminescence signals. TL signals are measured with no preheating, whereas OSL (blue stimulated), IRSL (infrared stimulated: IR_{50} and $pIRIR_{225}$) have been measured after a preheat of 250 °C for 60 s. OSL is measured at 125 °C, IR_{50} at 50 °C, $pIRIR_{225}$ at 225 °C immediately after the preceding IR_{50} measurement. IRPL (Prasad et al., 2017; Kumar et al., and Kook et al., these proceedings) was measured (subsequent to the measurement of $pIRIR_{225}$) at room temperature for 10 s using 830 nm stimulation and two 925 nm long pass (LP) filters and one 950 band pass (BP) filter; this configuration gives IRPL detection from 925 to 975 nm (1.3 eV band). The IRPL signal was placed after the IRSL measurements so that the IRSL signals would be unaffected by the IR stimulation during IRPL measurement.

3. Results

3.1. Quartzite

An optical image of the quartzite sample is given in Fig. 1a. The μXRF measurements show, not surprisingly, that the surface is dominated by silicon (Si, Fig. 1d) with an average concentration of 46.6% (cf. 46.7% for SiO_2, see Table S1). Nevertheless, there are some small regions where there are significant potassium (K, Fig. 1e) and sodium (Na, Fig. 1f) concentrations. Close examination of the Si map shows that there are corresponding small areas which appear darker than the main surface, i.e. areas where the Si concentration is reduced. The minor element images (Na and K) were analysed using optical density and an arbitrary threshold was set to discriminate against background. The resulting images were then overlain on the Si matrix image. The regions with significant Na concentrations match the areas of lower Si concentrations (Fig. S2). However, this does not apply to the K-rich regions, perhaps because of the higher energy of the 3.3 keV potassium K_α-line (i.e. because of the different X-ray energies, the Na_α 1.0 keV-line originates within the top 2–3 μm of the samples, whereas that from potassium is more penetrating, and originates within the top 20–25 μm).

Fig. 1b and c show the spatially resolved luminescence images of the 110 °C TL peak and the blue stimulated OSL, respectively, both detected in the UV. The TL image was derived by summing the light detected between 90 and 120 °C and the OSL image by summing the first 4 s of stimulation. If we first compare the TL and OSL images it is clear that, in some regions of the rock slice, there is a correlation between TL and OSL, i.e. intense TL corresponds to intense OSL (see the black dashed circles). However, there are also areas with intense TL but no discernible OSL (red ellipses). So some regions of the quartzite slice give both TL and OSL, whereas others only give TL. This observation may provide a least part of the explanation for the intercepts in the well-known linear correlations between TL from the 110 °C peak and blue stimulated - OSL from quartz (e.g. Murray and Roberts, 1998).

3.2. Alkali feldspar

Fig. 2 summarises the results obtained from a slice of alkali feldspar with an average K concentration of 11.7% (measured using μXRF and positioned on a ternary diagram in Fig. 2c). In the optical image (Fig. 2a) one can visually identify lighter and darker regions. Fig. 2b shows the elemental composition map of K and Na. Not surprisingly for a K-rich feldspar the surface is dominated by potassium (pink areas in Fig. 2b). The average concentration for the pink areas is

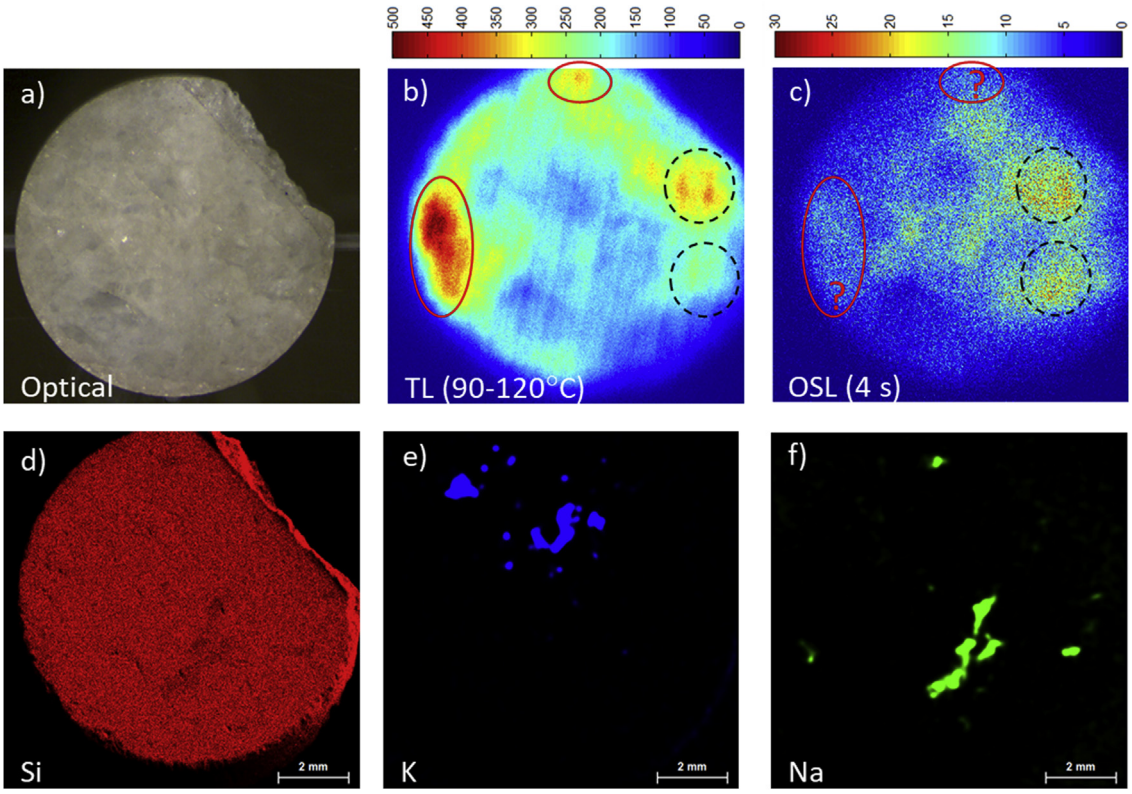

Fig. 1. Quartzite sample. a) Optical image, b) Spatially resolved TL image. The sample was given a dose of 40 Gy and subsequently heated to 250 °C at 1 °C/s (UV-detection). The TL signal was then summed from 90 to 120 °C, c) Spatially resolved OSL (blue stimulation) image. The image was obtained immediately after b) and has been obtained by summing the first 4 s of the OSL signal, d) Silicon (Si) map, e) Potassium (K) map, f) Sodium (Na) map. The black dashed circles in b) and c) indicate regions with both TL and OSL emissions, whereas the red ellipses indicate areas with intense TL but no OSL emission. (For interpretation of the references to colour in this figure legend, the reader is referred to the Web version of this article.)

13.93 ± 0.05% (n = 9) suggesting a matrix of essentially pure orthoclase. However, there are also small but significant areas dominated by sodium (green areas in Fig. 2b, average Na concentration of 6.8 ± 0.4%, n = 8, cf. Na in albite 8.8%). These occur in localised regions with low K concentrations and are an example of the well-known exsolution of albite in K-feldspars giving rise to the perthite structure visible in the optical image (Fig. 2a). The lighter regions in the optical image correlate with the regions with low K concentration and high Na concentration (see e.g. the area marked with a black oval in Fig. 2). The Ca (Calcium), Na and K elemental maps are given separately in Figs. S3a,b,c, respectively.

Fig. 2d,e,f show the TL, IR_{50} and $pIRIR_{225}$ luminescence images, respectively. Common to all images is that the luminescence is not uniformly distributed across the slice, i.e. there are clearly both dim and bright regions arranged in a linear pattern. There is a correlation between the dimmer luminescence areas and higher Na concentration (see Fig. S2 where the elemental map for Na overlies the IR_{50} image). Conversely, the bright areas correlate with the potassium-rich regions.

3.3. Granite rock samples

The optical image, a compositional map of the dominating element (iron, silicon, aluminium, potassium and sodium) and four luminescence images (TL, IR_{50}, $pIRIR_{225}$ and IRPL) for the Granite I rock slice are shown in Fig. 3. From the optical image alone, it is clear that different mineral regions are present in the slice. If we compare the optical image (Fig. 3a) with the iron (Fe) concentration (yellow regions in Fig. 3b), it is clear that these iron-dominated areas correspond to the darker patches in the optical image. The silicon-dominated regions (cyan regions in Fig. 3b) mainly represent quartz. K-rich (red) and Na-rich (green) regions are superimposed on the Al-rich regions (blue); the Si-rich overlapping regions mainly represent K- and Na-feldspars.

3.3.1. Spatially resolved TL (granite I)

The inset to Fig. 4 shows the TL curve to 250 °C (1 °C/s) as recorded by the standard PMT, i.e. the counts originate from the entire sample with no spatial information. The corresponding spatially resolved TL image shown in Fig. 3c has been obtained by summing the counts detected in the temperature range of 140–141 °C (note that the TL signal from this sample is bright and the appearance of the graph does not change significantly if a wider summation interval is chosen). It appears that TL is not emitted uniformly from this sample. If we compare the spatially resolved TL image with, for instance, the regions identified as iron-rich (yellow in Fig. 3b), it can be deduced that these are not responsible for the TL. This is shown more clearly in Fig. 4, where the data have been summed over 20 pixels (giving n = 12,996) and the resulting integrated TL intensities plotted against the iron-concentrations; the inverse-correlation is clear. However, these data are somewhat misleading, because the very high density of points at low TL intensities is not readily visible; furthermore, the density of data for a given concentration are biased by how frequently that concentration is observed on the sample (i.e. weighting by area). In the top panel of Fig. 4, the frequency distribution of the measured concentrations is given to clarify this issue. To obtain a clearer view of the correlation between a signal and the elemental composition, one needs to normalise for area. Thus, we binned the luminescence intensity data in intervals of 0.7% of the range of the Fe concentrations and averaged the intensity in each bin. This gives the solid curve (red) in Fig. 4. Finally, it must be born in mind that because some of the areas of the iron-rich regions appear to be comparable to (and presumably also less than) the optical resolution of our luminescence measurement system (i.e. ~20 μm), then when a small Fe-rich region is adjacent to e.g. a high K-

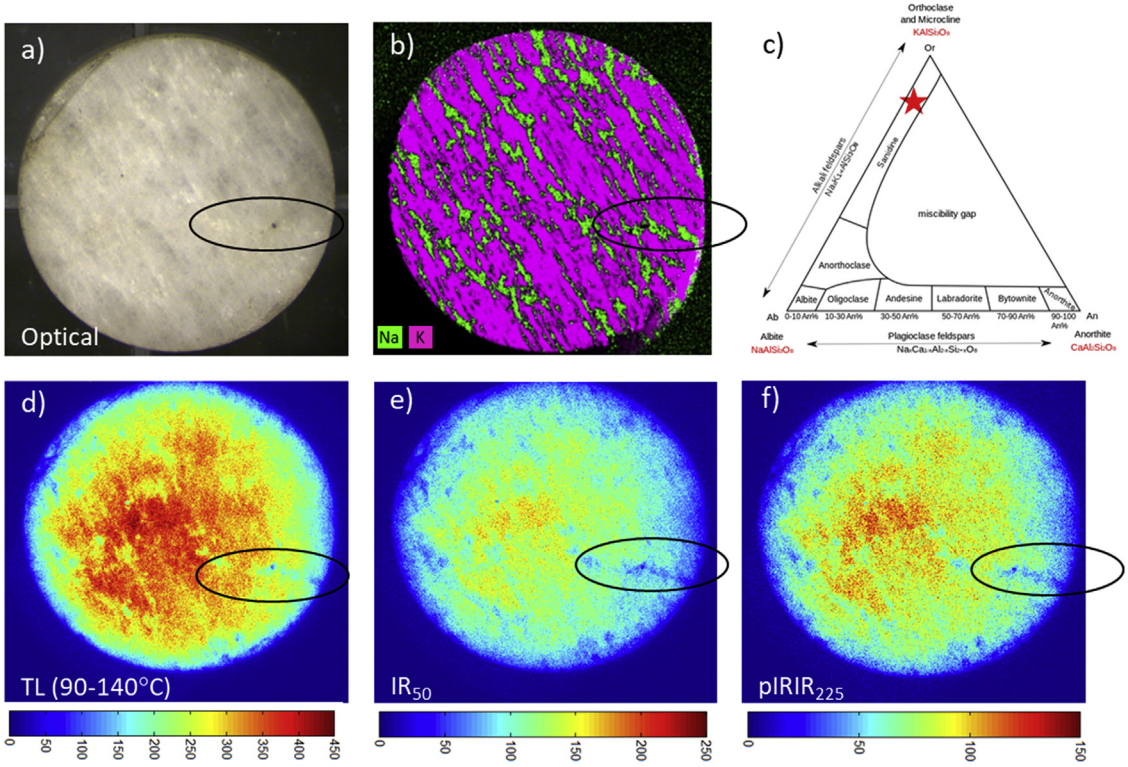

Fig. 2. Alkali feldspar rock sample. a) Optical image, b) Sodium and potassium elemental map, c) Average position of the sample on the ternary diagram is shown by the red star, d) Spatially resolved TL image for the temperature range 90–140 °C, e) Spatially resolved IRSL measured at 50 °C (IR_{50}) image for the first 10 s of stimulation after a given dose of 60 Gy and a preheat to 250 °C held for 60 s, f) Spatially resolved IRSL at elevated (225 °C) temperature ($pIRIR_{225}$) image for the first 10 s of stimulation. (For interpretation of the references to colour in this figure legend, the reader is referred to the Web version of this article.)

concentration region there is some breakthrough of the luminescence signal. This accounts for the outliers in Fig. 4 and probably explains why the solid curve in Fig. 4 seems to suggest that intermediate Fe-concentrations give significant luminescence.

In Fig. 5a the relationship between the average luminescence intensity of the four measured luminescence signals (TL, IR_{50}, $pIRIR_{225}$ and IRPL) are shown as a function of K concentration (K map shown in Fig. S4a). The TL signal appears to come almost entirely from K concentrations greater than ~8% K (14% correspond to the stoichiometry of pure K-feldspar).

The TL relationship with Na (Fig. 5b; Na map in Fig. S4b) shows that TL is predominantly emitted from regions with low Na concentrations (i.e. between 0 and 2%), presumably associated with high K concentration regions. High Na concentrations do not appear to give rise to significant TL signals.

3.3.2. *Spatially resolved IRSL (IR_{50}, granite I)*

Spectrometer measurements were undertaken to confirm that the blue IRSL emission at 50 °C (Fig. 6a) lies in the same spectral region as TL (see section 2.1). Unfortunately, because of the presence of the IR stimulation light, it was necessary to make this measurement through a BG39 band pass filter FWHM from ~340 to 610 nm; we have confirmed that this filter does not dictate the shape of the observed spectrum except that it prevents us from examining the UV emission below 340 nm. From Fig. 6a we deduce that our existing blue filter combination (long wavelengths dominated by BG-3 band pass filter with FWHM from ~275 to 470 nm) covers the blue IR emission, centred on 400 nm.

The IR_{50} signal (Fig. 3d) originates from regions with both high and low K concentrations (Fig. 5a). However, if we compare the Na-rich areas with the IR_{50} signal (see Fig. 5b), then it is clear that bright IR_{50} signals in the blue band are emitted from both K- and Na-rich regions. We note that Huntley et al. (1989, 1991), Jungner and Huntley (1991), Bailiff and Poolton (1991) and Huntley and Baril (1997) all suggest that K-feldspars emit mainly in a broad blue-band centred on ~400 nm, while Na-rich feldspars emit mainly in a band centred on 570 nm; however, since blue emission is not excluded, this is not necessary in conflict with our observation (see also Fig. 6a). In any case, our observation has important dosimetric implications, as a dose measured using the blue IRSL signal in rocks may derive from both Na-rich and K-rich areas, but the dose rate to a Na-rich feldspar should be lower than that to a K-rich feldspar, by about 35% for a 180–250 μm K-feldspar grain in a typical matrix containing 5, 4 and 355 Bq/kg of U, Th, K, respectively (Ankjærgaard and Murray, 2006).

Fig. 7a shows the average IR_{50} intensity in bins of width 0.7% (Si) and 0.1% (Ca). There is a well-defined broad IR_{50} peak at ~30% Si, presumably corresponding to K- and/or Na-rich feldspar (cf. expected values for orthoclase and albite of 30.3 and 32.1%, respectively). The apparent peaks at ~10 and 12% are almost certainly noise (they are based on the average of only 140 and 320 pixels, respectively, whereas the main peak at 30% is based on ~85,000 pixels). There is a similar well-defined peak (possibly at doublet) in the Ca data at ~3.6%. If most of this Ca is present as Ca-rich feldspars then this might suggest a mixture of 24% Ca-rich feldspar and 76% Na-rich feldspar, but this is speculative.

An alternative way of examining these data is to examine the dependence of the Si and Ca concentration distributions on the presence or absence of an IR_{50} signal. Fig. 7b show the Si concentration frequency distribution (black data). There are distinct peaks at ~0, ~17, 29.0, 30.0 and 46.4%. The latter peak presumably represent quartz, which has an expected Si concentration of 46.7%. If only the concentrations for which the IR_{50} signal is detectable are selected (here arbitrarily chosen to be > 10% of the maximum IR_{50} intensity, red data), the peaks at ~0, ~17 and 46.4% almost disappear, giving us

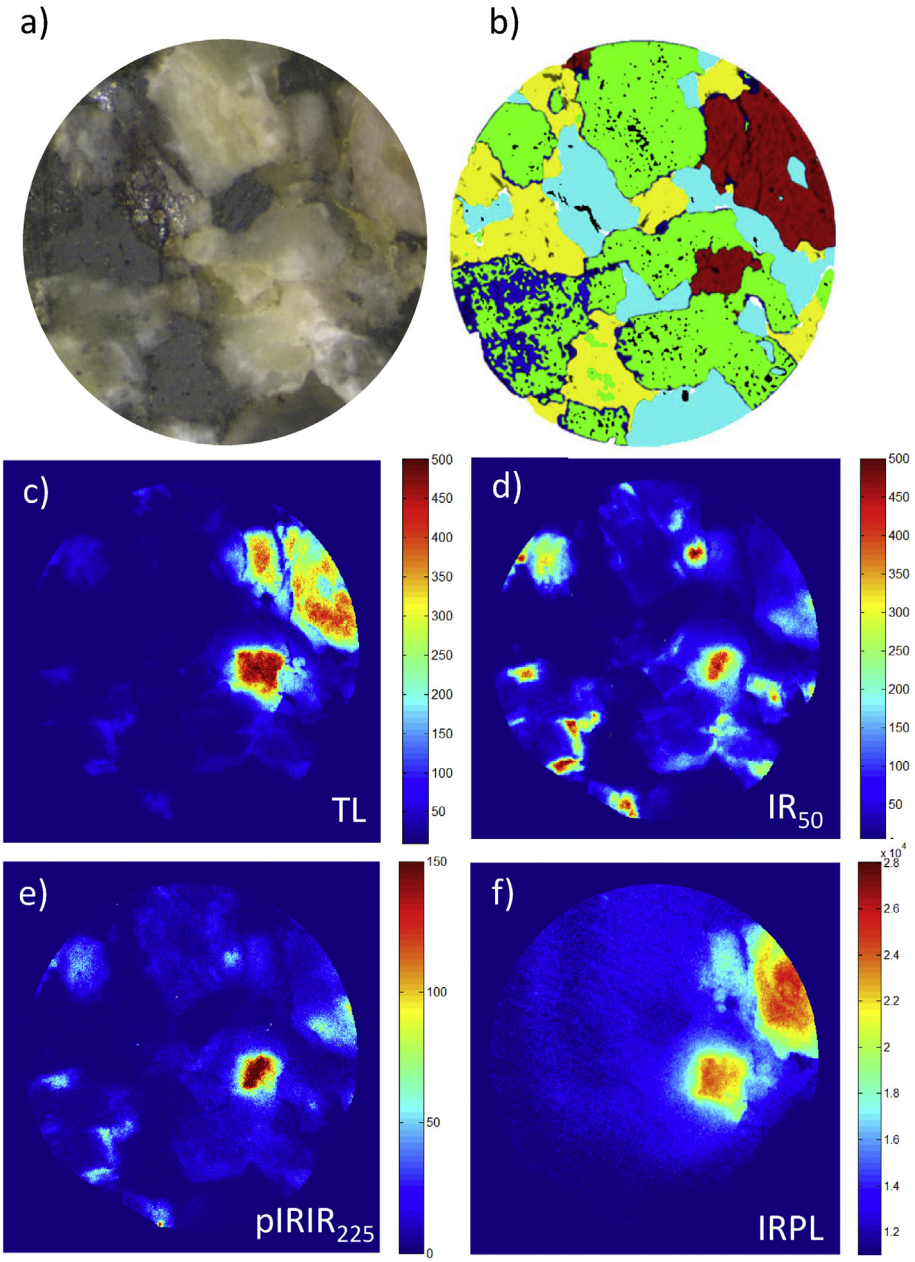

Fig. 3. Granite I rock slice. a) Optical image, b) Combined major element map. Iron (Fe): yellow, Silicon (Si): cyan, aluminium (Al): blue, potassium (K): red and sodium (Na): green, c) Spatially resolved TL image for the temperature range 140–141 °C. The sample was given a laboratory dose of 700 Gy and TL was recorded until 250 °C and the temperature held for 50 s, d) Spatially resolved IRSL (measured at 50 °C) image for the first 50 s of stimulation obtained immediately after c), e) Spatially resolved IRSL at elevated (225 °C) temperature image for the first 50 s of stimulation. The image was obtained immediately after d), f) IRPL for 1 s of summation. Background subtraction has been used for the IRPL image only. (For interpretation of the references to colour in this figure legend, the reader is referred to the Web version of this article.)

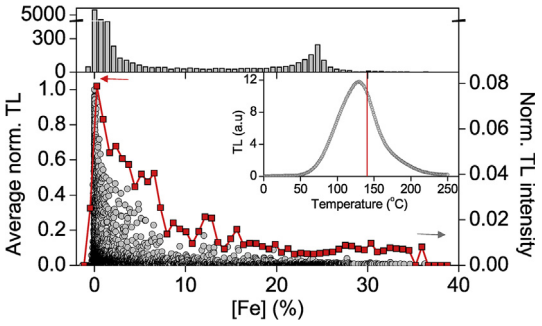

Fig. 4. Granite I rock slice. Correlation between TL intensity (summed from 140 to 141 °C) and iron (Fe) concentration (grey circles). Also shown is the average normalised TL intensity in bins of 0.7% widths (red squares). The inset shows the TL glow curve measured with a PMT after giving a laboratory dose of 700 Gy. The top panel shows the frequency distribution of measured Fe concentrations. (For interpretation of the references to colour in this figure legend, the reader is referred to the Web version of this article.)

further confidence that the 46.4% peak does in fact correspond to quartz. The very sharp peak at 30.0% and the broader peak at 29.0% remain pronounced after the application of this threshold. The peak at 30.0% presumably corresponds to orthoclase (cf. expected Si concentration of 30.3%). Similar calculations using Al (Fig. S5) also show a pronounced peak at 9.7% (cf. expected Al concentration in orthoclase of 9.7%). The broader Si peak at 29.0% presumably represent mixtures of Na- and Ca-rich feldspars (expected values of 32.1 and 20.2% for albite and anorthite, respectively). If so then we would expect these mixtures on average to consist of 26% Ca-rich feldspars and 74% Na-rich feldspars, supporting the more speculative values derived above.

Fig. 7c shows the corresponding frequency distribution for Ca concentrations. In the unfiltered (black) data there are two distinct peaks at 3.5 and 3.9% sitting on a very strong broad background. If these data are filtered as above then the two distinct peaks remain and much of the background is removed. Assuming that the peaks at 3.5 and 3.9% represent Ca-rich feldspars this would suggest the presence of mixtures (presumably with Na) of 24.3 and 27.1%, respectively, very similar to

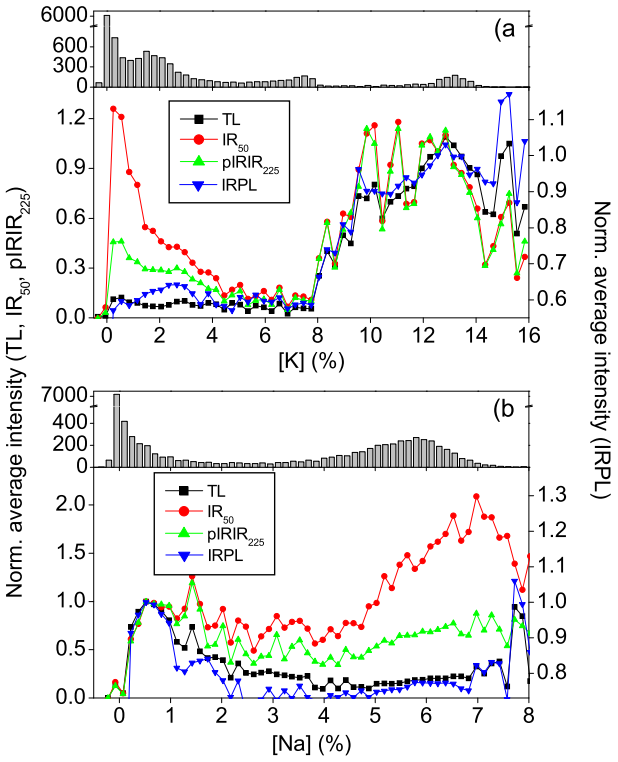

Fig. 5. Granite I rock slice. Normalised average luminescence intensity (TL, IR50, pIRIR225 and IRPL) vs concentration. The data has been derived from that presented in Fig. 3. Note that the IRPL data are plotted on a separate vertical scale and have been off-set to compensate for stimulation light breakthrough. Square symbols (black): TL; filled circles (red): IR_{50}; upward facing triangles (green): $pIRIR_{225}$; downward facing triangles (blue): IRPL. a) Potassium concentration. b) Sodium concentration. The top panels show the frequency distributions of measured concentrations. (For interpretation of the references to colour in this figure legend, the reader is referred to the Web version of this article.)

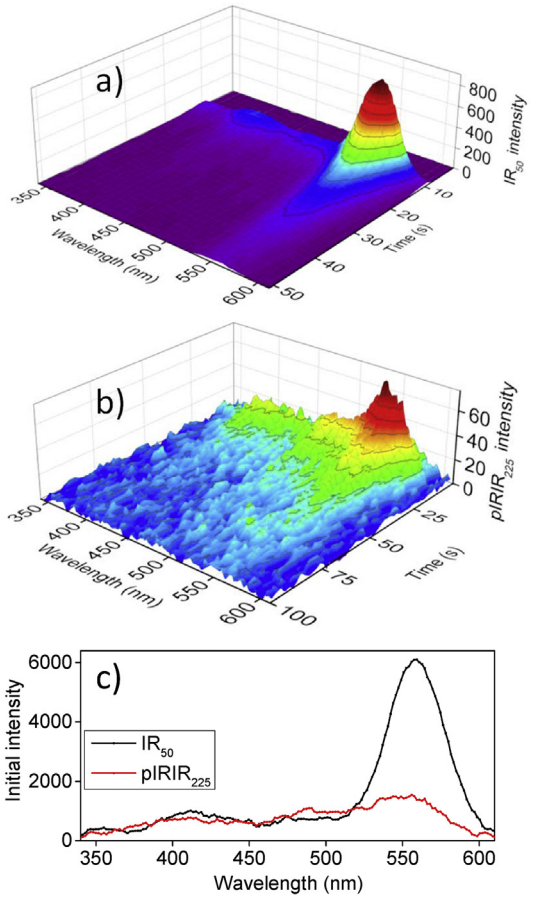

Fig. 6. IRSL spectrometer measurements for the granite I rock slice. Emission wavelength is shown on the x-axis, stimulation time on the y-axis and the luminescence intensity on the z-axis. a) IR_{50}, b) $pIRIR_{225}$, c) IR_{50} and $pIRIR_{225}$ for the first 1 s of stimulation.

the 26% identified from the Si data (see above). Similar calculations using Al (Fig. S5) also give an average fraction of Ca-rich feldspar of 25.3%.

3.3.3. Spatially resolved IRSL at elevated temperature ($pIRIR_{225}$, granite I and granite II)

Fig. 3e shows the spatially resolved $pIRIR_{225}$ signal for sample Granite I. As was found for the IR_{50} signal, bright $pIRIR_{225}$ signals are observed from K-rich regions (Fig. 5a and Fig. S6). There is also some light from low K, Na-rich regions, but this is much less intense than the IR_{50} signal (Fig. 5a and b). A similar pattern is observed for the granite II sample (Fig. S7), which helps to demonstrate the generality of the observation. We conclude that the elevated temperature IRSL signal in these samples is more clearly associated with the K-rich regions (rather than with both the K-rich and Na-rich as is the case for the IR_{50} signal) suggesting that the dosimetry of the $pIRIR_{225}$ signal is less complicated than that of the IR_{50} signal.

3.3.4. Spatially resolved IRPL

Fig. 3f shows the spatially resolved IRPL signal (Prasad et al., 2017; Kumar et al., these proceedings; Kook et al., these proceedings). The correlation between IRPL signals and K concentrations is shown in Fig. 5a. As with the TL signal and to a lesser degree the $pIRIR_{225}$ signal, the brightest IRPL signals all arise from the regions with the highest K concentrations, suggesting that the dosimetry of the IRPL signal should be similar to that of the TL and $pIRIR_{225}$ signal. The IRPL signal arises from all IR sensitive electron traps, both stable and unstable. In this experiment the less stable IRPL signals (corresponding to the traps giving rise to low temperature IRSL) are already likely to have been eliminated by the prior $pIRIR_{225}$ measurement. The relationship of the IRPL signal to the Na-concentration is very similar to that of the TL.

4. Conclusion

We have presented spatially resolved luminescence and concentration data obtained from 4 rock slices that clearly show the relationships between quartz and feldspathic regions and TL, OSL, IRSL and IRPL. In the case of the measurements using quartzite, it appears that only some of the regions that give the 110 °C TL peak also emit OSL, and this is a likely explanation of the well-known intercept in the relationship between these two signals.

The Norwegian alkali-feldspar sample shows clear evidence of exsolution, and the less common Na-rich regions produce significantly less intense IRSL than the corresponding K-rich regions. This relationship is not as clear in the granite sample from Denmark, where the IR_{50} signal appears to arise from both Na-rich and K-rich regions, but the TL signal, on the other hand, is predominantly from K-rich areas, with only a weak signal from Na. A comparison of the averaged IR_{50} signals with the Si and Ca concentrations also suggest that the IR_{50} is preferentially associated with Na- and K-rich feldspars and that Na and Ca may be mainly present in the ratio of ~0.75 to ~0.25. These tentative conclusions are strongly reinforced by using the presence or absence of IR_{50} to filter the Ca and Si concentrations.

The $pIRIR_{225}$ signal behaves similarly to the TL signal, although there is a slightly larger contribution from regions of low K concentration. The IRPL signal also behaves similarly, although it must be

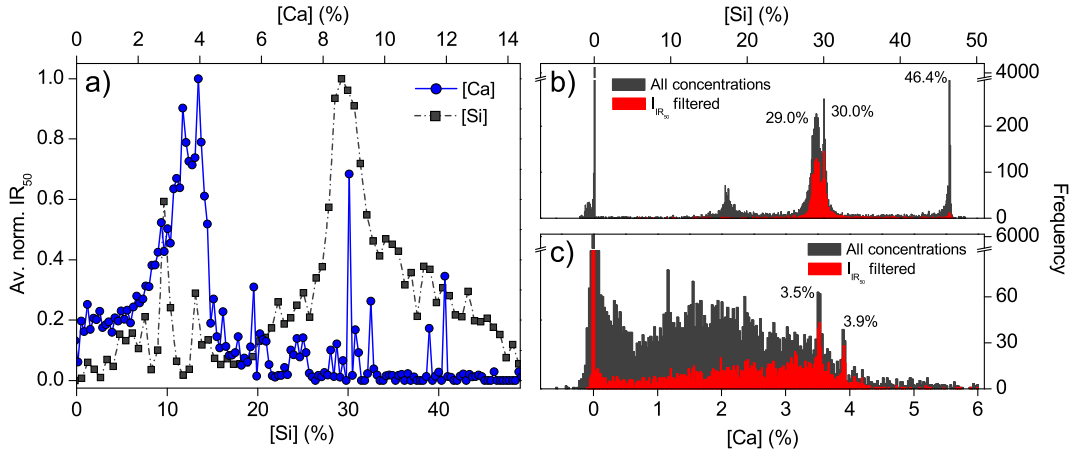

Fig. 7. Granite I rock slice. a) Scatter plots showing the average normalised IR_{50} intensity against Si concentration (grey squares, dotted line) and Ca concentration (blue circles, solid line).b), c) The histograms show the concentration frequency distributions of Si (b) and Ca (c). The red histograms show the concentration distribution for all pixels with an IR_{50} intensity larger than 10% of the maximum intensity. (For interpretation of the references to colour in this figure legend, the reader is referred to the Web version of this article.)

remembered that the IRPL was measured following the IR_{50} and $pIRIR_{225}$ measurements, and so does not include any less stable component.

All of these observations relate to signal intensity, not dose. By spatially selecting different regions of the rock surface, dose can be derived from systems that are likely to be dosimetrically simpler than had the integral signal been used. It seems appropriate to continue to use the assumption of 12.5% K for the dosimetry of the $pIRIR_{225}$ signal when dating K-rich feldspar extracts from sediment, but perhaps a lower K concentration when dating rock slices using the integrated IR_{50} signal. The latter is probably of less concern when dating sediments because the more easily weathered Na-feldspars are usually present only in very low concentrations.

It is clear that there is a considerable amount of luminescence and dosimetric information to be gained from the combination of spatial imaging of luminescence and elemental concentrations. The challenge will be to automate the data reduction so that such investigations can become integrated into routine measurements.

Acknowledgements

Funding from the European Research Council under the European Union Horizon 2020 research and innovation programme ERC-2014-StG 639904 – RELOS is acknowledged.

Appendix A. Supplementary data

Supplementary data related to this article can be found at http://dx.doi.org/10.1016/j.radmeas.2018.06.002.

References

Ankjærgaard, C., Murray, A.S., 2006. Total beta and gamma dose rates based on beta counting in trapped charge dating. Radiat. Meas. 42, 352–359.
Bailiff, I.K., Poolton, N.R.J., 1991. Studies of charge transfer mechanisms in feldspars. Nucl. Tracks Radiat. Meas. 18, 111–118.
Buylaert, J.-P., Újvári, G., Murray, A.S., Smedley, R.K., Kook, M., submitted. On the relationship between K concentration, grain size and dose in feldspar. Radiation Measurements, these proceedings.
Bøtter-Jensen, L., Thomsen, K.J., Jain, M., 2010. Review of optically stimulated luminescence (OSL) instrumental developments for retrospective dosimetry. Radiat. Meas. 45, 253–257.
Bøtter-Jensen, L., Duller, G.A.T., Poolton, N.R.J., 1994. Excitation and emission spectrometry of stimulated luminescence from quartz and feldspars. Radiat. Meas. 23, 613–616.
Flude, S., Hasche, M., Storey, M., 2017. Application of benchtop micro-XRF to geological materials. Mineral. Mag. 81 (4), 923–948.
Huntley, D.J., Baril, M.R., 1997. The K content of the K-feldspars being measured in optical dating or in thermoluminescence dating. Ancient TL 5, 11–13.
Huntley, D.J., Godfrey-Smith, D.I., Haskell, E.H., 1991. Light-induced emission spectra from some quartz and feldspars. Int. J. Radiat. Appl. Instrum. D. Nucl. Tracks. Radiat. Meas. 18, 127–131.
Huntley, D.J., McMullan, W.G., Godfrey-Smith, D.I., Thewalt, M.L.W., 1989. Time-dependent recombination spectra arising from optical ejection of trapped charges in feldspars. J. Lumin. 414, 41–46.
Jungner, H., Huntley, D.J., 1991. Emission spectra of some potassium feldspars under 633 nm stimulation. Nucl. Tracks Radiat. Meas. 18, 125–126.
Kook, M., Kumar, R., Murray, A.S., Thomsen, K.J., Jain, M., submitted. Instrumentation for the non-destructive optical measurement of trapped electrons in feldspar. Radiation Measurements, these proceedings.
Kook, M., Lapp, T., Murray, A.S., Thomsen, K.J., Jain, M., 2015. A luminescence imaging system for the routine measurement of single-grain OSL dose distributions. Radiat. Meas. 81, 171–177.
Kumar, R., Kook, M., Murray, A.S., Jain, M., submitted. Towards direct measurement of metastable (trapped) electrons in K-feldspar: Do infrared- photoluminescence (IRPL) and radioluminescence (IR-RL) probe the same trap? Radiation Measurements, these proceedings.
Lapp, T., Kook, M., Murray, A.S., Thomsen, K.J., Buylaert, J.-P., Jain, M., 2015. A new luminescence detection and stimulation head for the Risø TL/OSL reader. Radiat. Meas. 81, 178–184.
Murray, A.S., Roberts, R.G., 1998. Measurement of equivalent dose in quartz using a regenerative-dose single-aliquot protocol. Radiat. Meas. 29, 503–515. http://dx.doi.org/10.1016/S1350-4487(98)00044-4.
Prasad, A.K., Poolton, N.R.J., Kook, M., Jain, M., 2017. Optical dating in a new light: a direct, non-destructive probe of trapped electrons. Sci. Rep. 7http://dx.doi.org/10.1038/s41598-017-10174-8. Article number: 12097.
Prasad, A.K., Lapp, T., Kook, M., Jain, M., 2016. Probing luminescence centers in Na rich feldspar. Radiat. Meas. 90, 292–297.
Prescott, J.R., Hutton, J.T., 1994. Cosmic ray contributions to dose rates for luminescence and ESR dating: large depths and long-term variations. Radiat. Meas. 23, 497–500.
Smedley, R.K., Pearce, N.J.G., 2016. Internal U, Th and Rb concentrations of alkali-feldspar grains: implications for luminescence dating. Quat. Geochronol. 35, 16–25.
Thomsen, K.J., Kook, M., Murray, A.S., Jain, M., Lapp, T., 2015. Single-grain results from an EMCCD-based imaging system. Radiat. Meas. 81, 185–191.
Thomsen, K.J., Murray, A.S., Jain, M., Bøtter-Jensen, L., 2008. Laboratory fading rates of various luminescence signals from feldspar-rich sediment extracts. Radiat. Meas. 43, 1474–1486.
Trauerstein, M., Lowick, S., Preusser, F., Rufer, D., Schlunegger, F., 2012. Exploring fading in single grain feldspar IRSL measurements. Quat. Geochronol. 10, 327–333. http://dx.doi.org/10.1016/j.quageo.2012.02.004.